Electronic Supplementary Information (ESI)

# Stabilization of Fast Lithium-ionic Conduction Phase of Nanoconfined $LiBH_4$ for Lithium Metal Solid-State Batteries†

Shunqin Zeng, [ab] Kaixiang Ren,[a] Hongfei Ding,*[a] Shendong Xu *[c] Hai-Wen Li,[d] Yongtao Li, *[ae]

[a] *School of Materials Science and Engineering, Anhui University of Technology, Maanshan, 243002, China.*

[b] *College of Chemistry and Materials Engineering, Huaihua University, Huaihua,418000, China.*

[c] *School of Carbon Neutrality Science and Engineering, Anhui University of Science and Technology, Hefei 231131, P. R. China*

[d] *School of Advanced Energy, Sun Yat-Sen University, Shenzhen 518107, China.*

[e] *Key Laboratory of Green Fabrication and Surface Technology of Advanced Metal Materials of Ministry of Education, Anhui University of Technology, Maanshan 243002, China*

## MATERIALS AND METHODS

Commercial $LiBH_4$ powder (purity＞95%, Aladdin) without further purification. γ-$Al_2O_3$, mesoporous-$Al_2O_3$ (Meso-$Al_2O_3$) and α-$Al_2O_3$ (purity＞99%, all from Aladdin) are used after drying for 12 hours under dynamic vacuum conditions at 300 °C, to remove adsorbed water and oxygen. The $LiBH_4$/Meso-$Al_2O_3$ mixture was prepared in five different mixing ratios: 10 wt%, 25 wt%, 40 wt%, 55 wt% and 70 wt% of $LiBH_4$. To retain the pore structure of mesoporous alumina, the mixture is mixed by hand using a mortar and pestle, and then transferred to a stainless-steel crucible (10 mm diameter, 10 mm height) in a sealed stainless-steel heat-treated tube (18 mm diameter, 300 mm height) under an $H_2$ atmosphere of 5 MPa and heated at 295°C for 3 hours for molten penetration. To emphasize the effect of nanoconfined, we used pristine $LiBH_4$ and hand physical mixture as a control group.

As two control experiments, 25 wt% $LiBH_4$/α-$Al_2O_3$ and 25 wt% $LiBH_4$/γ-$Al_2O_3$ composites were prepared by high-energy ball milling method. It is to achieve uniform mixing, destroy the pore structure of alumina, to eliminate the constraint effect. The composites mixed in a ratio of 25 wt% $LiBH_4$ and 75 wt% alumina scaffolding were prepared using a planetary ball mill (QM-1SP4, Nanjing) in an 100 mL alumina jar for 2 h at 400 rpm (30 min milling was repeated with an interval of 5 min，in order to overcome heating effects) with alumina balls and the ball-to-sample ratio of 40:1 under 5 MPa $H_2$ atmosphere. All operations of the sample during the experiment were carried out in an Ar atmosphere in the glove box ($\rho(O2) < 0.1$ppm, $\rho(H_2O) < 0.1$ppm).

## CHARACTERIZATION

X-ray diffraction (XRD) measurements were taken on the Rigaku MiniFlex 600 (Rigaku, Japan), the samples were sealed in a glass scaffolding with polyimide thin-film (10 mm) tape under an Ar atmosphere. Fourier transform infrared (FTIR) spectra were acquired in transmission mode using Bruker Vector 22. Raman spectra were obtained by Bruker Optics Senterra R200-L. Transmission electron microscopy (TEM) observations were made on JEOL JEM-2100F, coupled with Energy Dispersive Spectroscopy (EDS). Fourier transform infrared At Micromeritics ASAP2020, the specific surface area and pore volume of the samples were characterized by brunauer-emmet-teller (BET) and Barrett-Joyner-Halenda (BJH) methods. Solid-state NMR experiments were performed on the Bruker Ascend 600 MHz (14.1 T) with a resonance frequency of 233 MHz, 7Li. Bruker 3.2mm magic Angle rotating probe was used in the 15 kHz MAS experiment. Differential Scanning Calorimetry (DSC) measurements were performed with an apparatus from Mettler Toledo (HP DSC1).

Electrochemical impedance spectroscopy (EIS), Direct Current (DC) polarization and Cyclic voltammetry (CV) were tested using Solartron Electrochemical workstation. The ionic conductivity was measured by electrochemical

impedance spectroscopy (EIS). SS|SSE|SS (SS: stainless steel), frequency range is 1Hz ~ $10^{-6}$Hz. A The cells were assembled using a homemade Swagelok mold. The powder sample was cold pressed into pellets with a diameter of 10 mm and a thickness of ~1 mm (for Li-ion conduction measurements) and ~0.8 mm (for electrochemical stability and electrode compatibility measurements) was made by clod pressing the target materials under 10 MPa pressure. EIS measurement temperature range is 35 ~ 125℃, in order to ensure the temperature test error, each test interval residence time is 60 min. Calculate the ionic conductivity according to equation (1), where ***d*** is the thickness of the electrolyte pellets (mm), ***R*** is the resistance (Ω), and ***S*** is the contact area of the electrolyte pellets ($mm^2$).

$$\sigma_{Li+} = \frac{d}{SR} \qquad (1)$$

The activation energy (***E***a) was evaluated according to the Nernst-Einstein equation and the Arrhenius equation (2).

$$\ln \sigma T = -\frac{E_a}{K_B T} + C, \qquad (2)$$

where $\boldsymbol{\sigma}$ is conductivity, ***C*** is the pre-exponential factor, $\boldsymbol{K_B}$ is Boltzmann's constant, and ***T*** is the temperature (K). Direct Current polarization was conducted by applying a constant voltage of 10 mV for 1500 s. Cyclic voltammetry (CV) was performed by Li|SSE|SS (SSE: $LiBH_4$/Meso-$Al_2O_3$) with a scanning rate of 0.5 mV $s^{-1}$ at -0.2~6.0V. The critical current density and constant current deposition of Li|SSE|Li symmetrical battery was measured by NEWARE(CT-3008) battery test system. $TiS_2$ (99.9%, Sigma-Aldrich) and $LiBH_4$/Meso-$Al_2O_3$ powders were mixed in an agate mortar with a mass ratio of 3:1 as a composite positive electrode. Assemble the all-solid-state $TiS_2$|$LiBH_4$/Meso-$Al_2O_3$|Li battery. The battery test was performed at 60 ° C with a charge/discharge ratio of 0.5 ℃ and a voltage range of 1.6 V to 2.7 V using the NEWARE(CT-3008) battery test system.

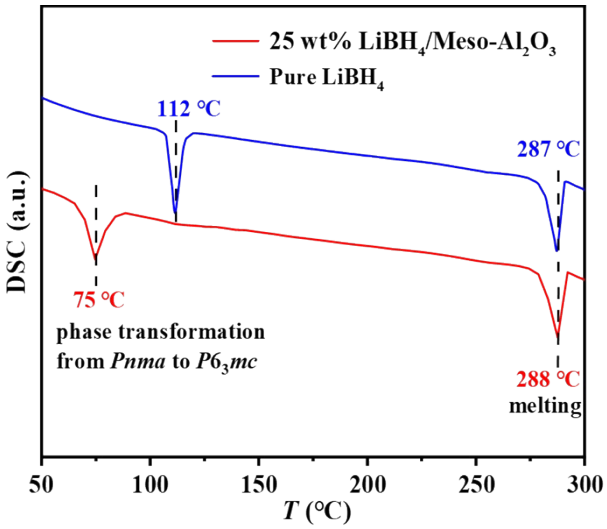


***Fig. S1***. DSC curves of 25 wt%$LiBH_4$/Meso-$Al_2O_3$ and pure $LiBH_4$.

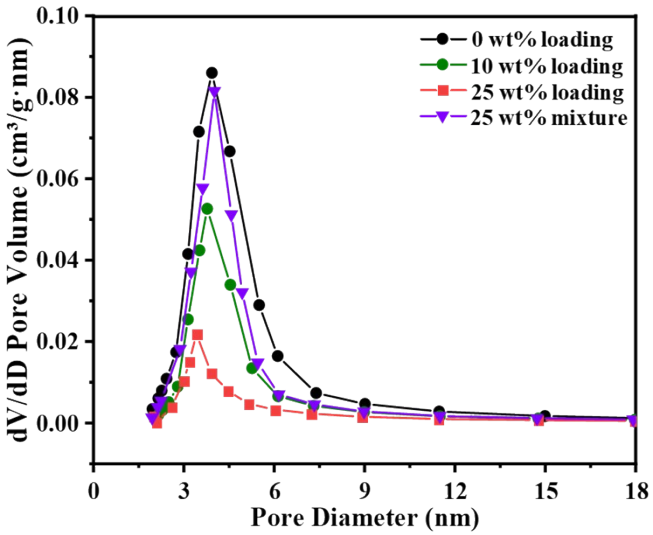


***Fig. S2***. Pore diameter of Meso-$Al_2O_3$, 25 wt%$LiBH_4$ mixture, 10 wt%$LiBH_4$ loading and 25 wt%$LiBH_4$ loading.

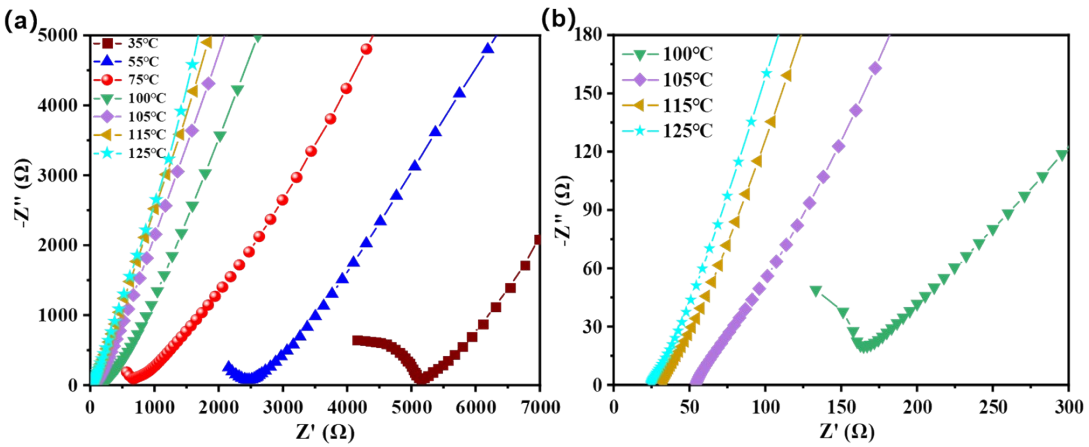


***Fig. S3***. (a) Representative Nyquist plots of 25 wt%$LiBH_4$/Meso-$Al_2O_3$ obtained from the EIS measurements at different temperatures. (b) shows the partial enlarged Nyquist plots of 25 wt%$LiBH_4$/Meso-$Al_2O_3$ from 100 to 125℃.

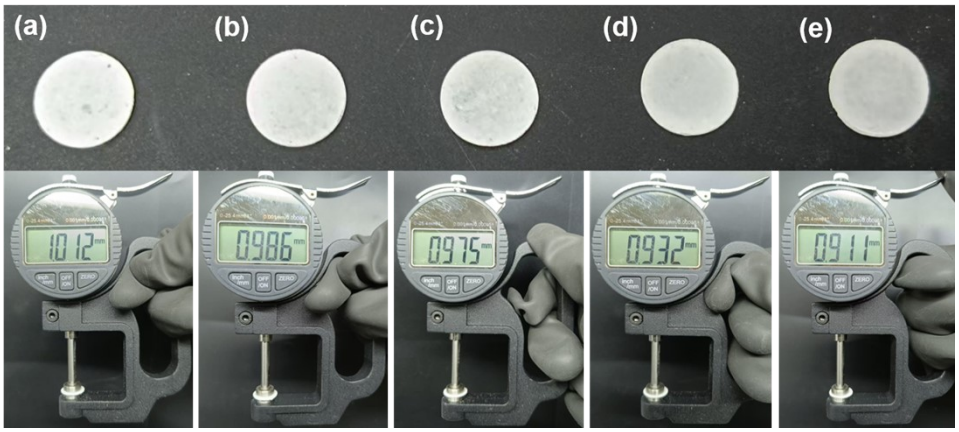


***Fig. S4***. Surface optical images and thicknesses of electrolyte pellets (a-e) 10 wt%, 25 wt%, 40 wt%, 55 wt%, 70 wt% of $LiBH_4$/Meso-$Al_2O_3$.

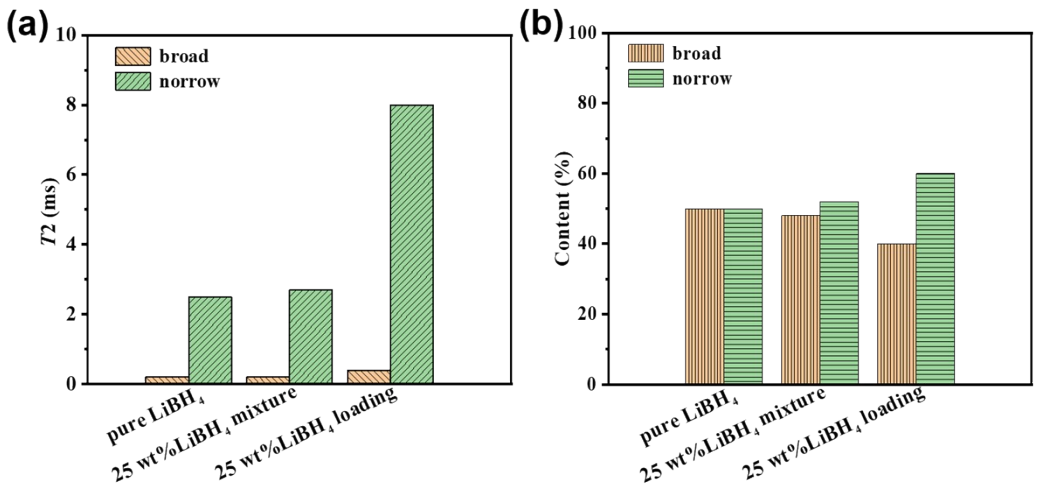


***Fig. S5***. (a)*T*2 and (a) contents of the narrow and broad NMR peaks at different samples.

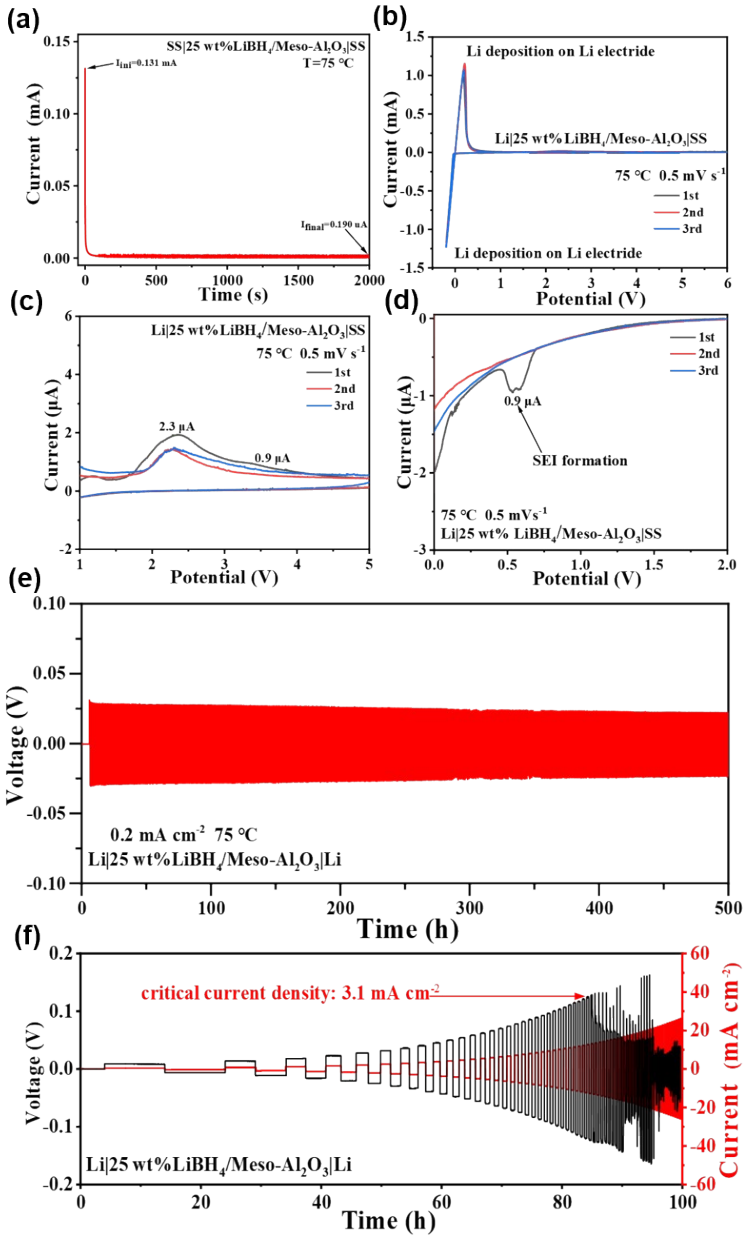


***Fig. S6*** (a) DC polarization curve; (b) CV curves; (c) enlarged zoom in view of the oxidation process and (d) the reduction process; (e) galvanostatic cycling curves of the electrochemical cells assembled with 25 wt%$LiBH_4$/Meso-$Al_2O_3$ electrolyte. (f) Stepped current density galvanostatic cycling for the Li|25 wt%$LiBH_4$/Meso-$Al_2O_3$|Li symmetric cell.

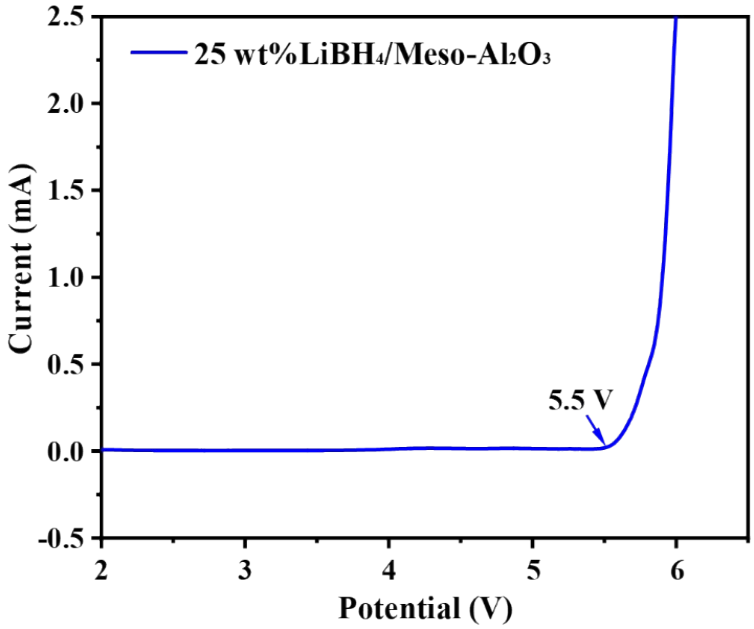


***Fig. S7***. Linear sweep voltammetry of 25 wt%$LiBH_4$/Meso-$Al_2O_3$ at 75℃.

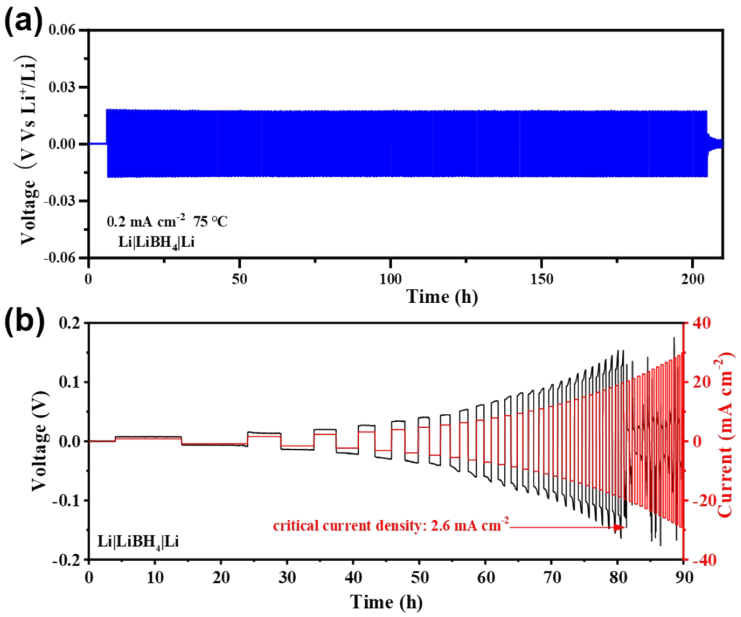


***Fig. S8***. (a) galvanostatic cycling curves of Li|$LiBH_4$|Li cell at 0.2 mA $cm^{-2}$. (b) stepped current density galvanostatic cycling for the Li|$LiBH_4$|Li symmetric cell.

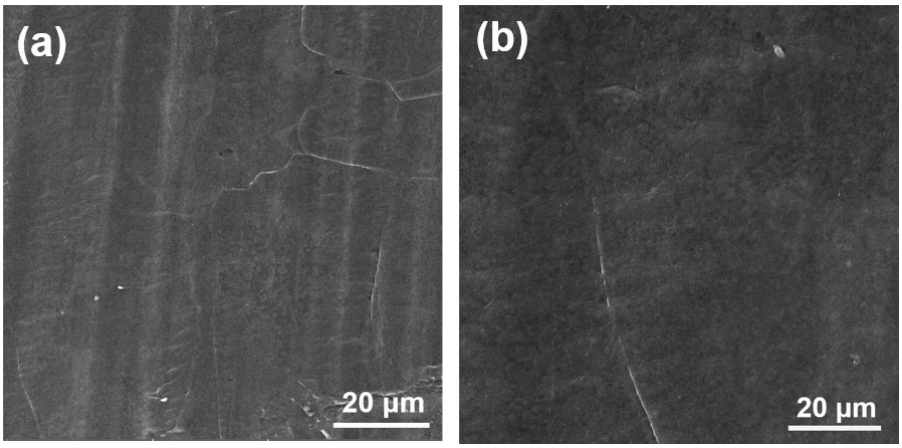


***Fig. S9***. SEM images of Li foil surface extracted from Li||Li cells before (a) and after (b) 500 h cycling with electrolyte of 25 wt% $LiBH_4$/Meso-$Al_2O_3$.

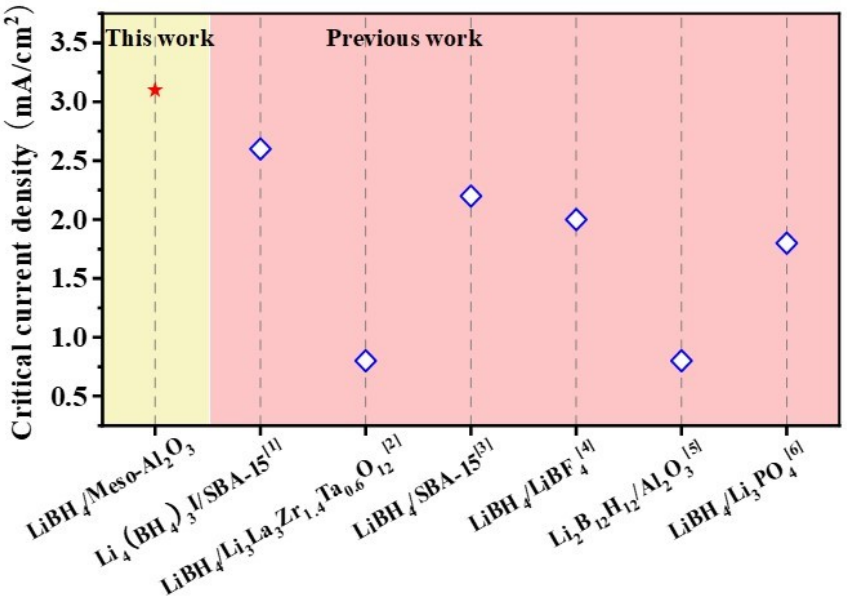


***Fig. S10*** The critical current density of solid electrolytes related to this work were compared.

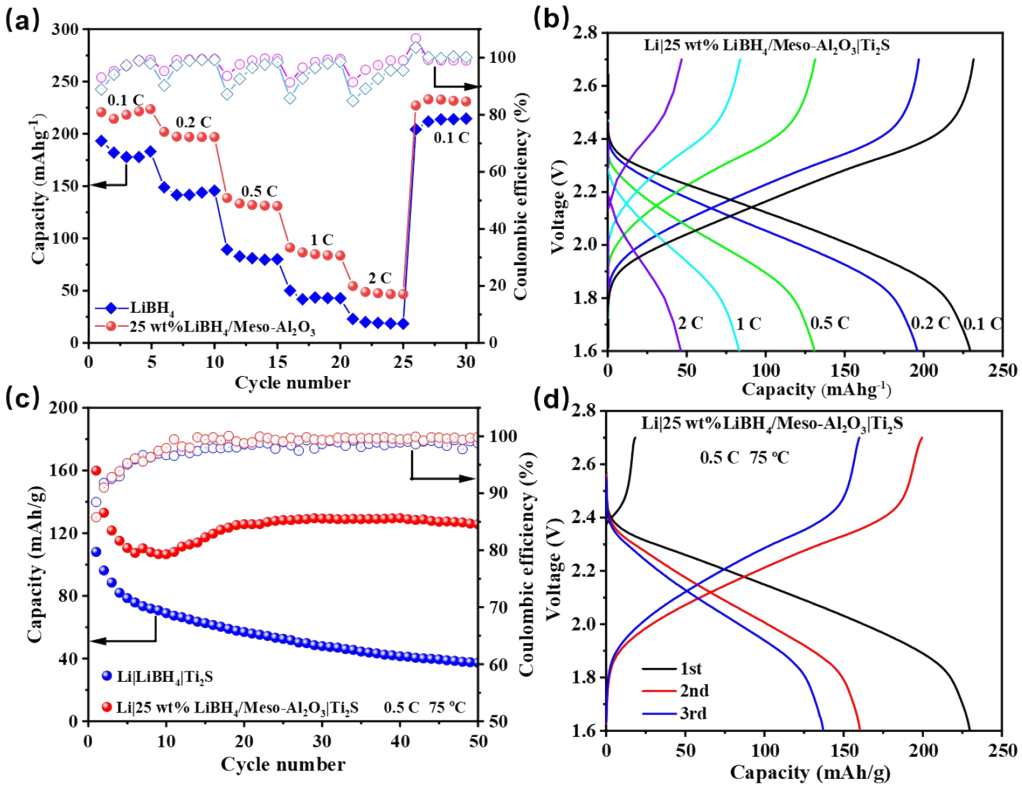


***Fig. S11*** (a) Corresponding specific capacities and the coulombic efficiency of Li|25 wt%$LiBH_4$/Meso-$Al_2O_3$|$Ti_2S$ and Li|$LiBH_4$ |$Ti_2S$ cells ranging from 0.1 to 2 C. (b) Typical Li|25 wt%$LiBH_4$/Meso-$Al_2O_3$|$Ti_2S$ charge/discharge curves at various rates. (c) The specific capacity and coulombic efficiency at 0.5 C for Li|25 wt%$LiBH_4$/Meso-$Al_2O_3$|$Ti_2S$ and Li|$LiBH_4$ |$Ti_2S$ cells during cycling. (d) corresponding Li|25wt%$LiBH_4$/Meso-$Al_2O_3$|$Ti_2S$ charge/discharge curves of the typical 1st, 2nd, 3rd, 40th, and 60th cycle at 0.5 C. All the electrochemical measurements were taken at 75 °C.

Fig. S11a shows the rate performance of Li|$LiBH_4$|$Ti_2S$ battery Li|25 wt%$LiBH_4$/Meso-$Al_2O_3$|$Ti_2S$ battery with every five cycles at 75°C. It can be clearly seen that Li|25 wt%$LiBH_4$/Meso-$Al_2O_3$|$Ti_2S$ provides high specific capacities of about 218.3, 197.1, 132.1, 84.8, and 47.6 mAh $g^{-1}$ at 0.1 C, 0.2 C, 0.5 C, 1.0 C, and 2.0 C, respectively. In comparison, the specific capacities of Li|$LiBH_4$|$Ti_2S$ batteries at the same magnification are 152.8, 140.8, 110.5, and 67.1 mAh $g^{-1}$. The detailed charge/discharge curves of Li|25 wt%$LiBH_4$/Meso-$Al_2O_3$|$Ti_2S$ ranging from 0.1 to 2 C are shown in Fig. S11b. To better illustrate the stability of the SSEs, Fig. S11c shows the cyclic performance of Li|25 wt%$LiBH_4$/Meso-$Al_2O_3$|$Ti_2S$ at 0.5C. The initial discharge capacity of current solid-state batteries is 107.5 mA h $g^{-1}$. After repeated activation, the specific capacity remained stable to 125.1 mA h $g^{-1}$. By contrast, the bare Li|$LiBH_4$|$TiS_2$ cells showed a sustained capacity degradation behavior at 0.5 C, which was attributed to more severe dendrite growth at high C-rates. As exhibited in Fig. S12 ESI†, The resistance of the Li|25 wt% $LiBH_4$/Meso-$Al_2O_3$|$TiS_2$ battery before cycling is ~550 Ω, which reduces to ~350 after the 50 cycles. However, the resistances of Li|$LiBH_4$|$TiS_2$ increased significantly after 50cycles. The low interfacial resistance of full cell with 25 wt%$LiBH_4$/Meso-$Al_2O_3$ is the result of higher ionic

conductivity, uniform lithium plating/stripping, and smaller polarization. SEI was formed during the discharge, which ensured that the battery could be relatively stable in subsequent cycles [7]. During the initial activation process, the $Li^+$ in the composite electrolyte is homogenized, and the rapid transport path of $Li^+$ is established [8]. At the same time, the contact between electrolyte and electrode material is improved, thus reducing the interface impedance between electrolyte and cathode [9]. As shown in Fig. S11d, Li|25 wt%$LiBH_4$/Meso-$Al_2O_3$|$Ti_2S$ charging and discharging curves under different cycles at 0.5 C. These results indicate that the stable interface could effectively protect the $Ti_2S$ cathode from decomposition during the charging and discharging process and improve the stability of the lithium metal anode.

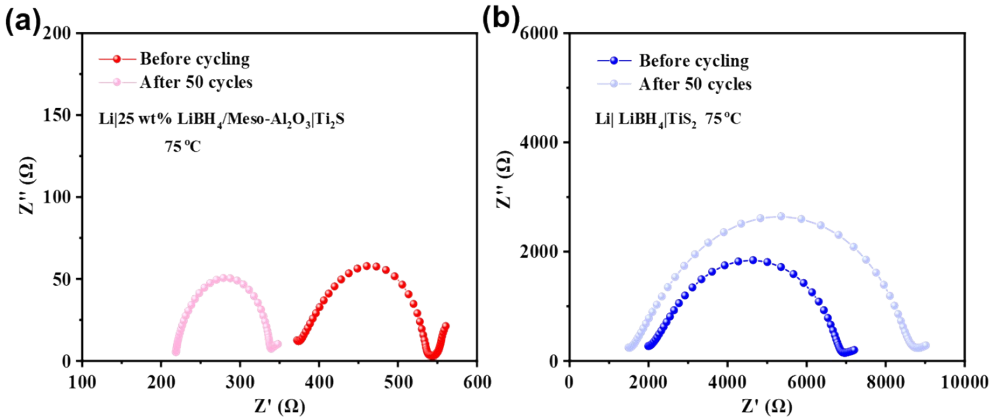


***Fig. S12.*** (a, b) EISs spectra of Li|25 wt%$LiBH_4$/Meso-$Al_2O_3$|$TiS_2$ and Li|$LiBH_4$|$TiS_2$ cells during different cycles of charge-discharge at 0.5 C. $Al_2O_3$|Li symmetric cell.

## Supplementary References


1. F. Q. Lu, Y. P. Pang, M. F. Zhu, F. D. Han, J. H. Yang, F. Fang, D. L. Sun, S. Y. Zheng and C. S. Wang, Adv. Funct. Mater., 2019, **29**, 1809219.
2. Y. Gao, S. Sun, X. Zhang, Y. Liu, J. Hu, Z. Huang, M. Gao, and H. Pan, *Adv. Funct. Mater.,* 2021, **31**, 2009692.
3. G. Yang, C. Xie, Y. Li, H. Li, D. Liu, J. Chen and Q. Zhang, *Dalton Trans.*, 2021,**50**, 15352-15358
4. X. Shi, Y. Pang, B. Wang, H. Sun, X. Wang, Y. Li, J. Yang, H-W. Li and S. Zheng, *Mater, Today Nano,* 2020, **10**, 100079
5. C. Y. Zhou, H. Sun, Q. Wang, J. B. Grinderslev, D. Liu, Y. G. Yan and T. R. Jensen, *J Alloy Compd.*, 2023, **938**, 168689.
6. S. Zeng, X. Ding, L. He, H. Li, Q. Zhang and Y. Li*, Mater. Adv.*, 2023, **4**, 2780-2784
7. Z. J. Bi, R. D. Shi, X. N. Liu, K. Y. Liu, M. Y. Jia and X. X. Guo, *Adv. Funct. Mater.,* 2023, **33**, 2307701.
8. Y. J. Tian, F. Ding, H. Zhong, C. Liu, Y. B. He, X. J. Liu and Q. Xu, *Energy Storage Mater.*, 2018, **14**, 49-57.
9. Z. Zhang and L. F. Nazar, *Nat. Rev. Mater.*, 2022, **7**, 389-405.